AIAA JOURNAL
Vol. 49, No. 5, May 2011

Computational Investigation of Three-Dimensional Unsteady Flowfield Characteristics Around Insects' Flapping Flight

Jin-Ho Kim* and Chongam Kim†
Seoul National University, Seoul 151-742, Republic of Korea

DOI: 10.2514/1.J050485

This paper investigates the unsteady flowfield characteristics around three-dimensional insect flapping motion under forward flight conditions. A realistic wing trajectory, called the "figure-of-eight" motion, is extracted from a blowfly's (*phormia regina*) tethered flight experiment under a freestream velocity of 2.75 m/s. In the authors' preliminary research [Lee, J., Kim, J., and Kim, C., "Numerical Study on the Unsteady-Force-Generation Mechanism of Insect Flapping Motion," *AIAA Journal*, Vol. 46, No. 7, 2008, pp. 1835–1848. doi:10.2514/1.35646], the two-dimensional blowfly's wing motion was computationally investigated, and the results revealed very interesting and distinctive vortical flowfields, which provide a decisive clue in understanding the rapid maneuverability of insects' flight. On the line of continuous efforts, the present work investigates the role of three-dimensional vortical structure in unsteady aerodynamic force generation. Detailed numerical simulation and analysis on three-dimensional flapping motion are conducted, and interesting flow features of insects' flapping flight are observed, such as the existence of a spanwise flow component, leading-edge vortex, wing tip vortex, trailing-edge vortex, and various forms of vortex tubes and vortex rings. It turns out that vortical structures play a crucial role in determining unsteady characteristics of lift and thrust generation. In particular, the vortex pairing and vortex staying phenomena, which have been observed in two-dimensional flapping motion, are also observed but with a more complicated pattern. On top of that, distinctive lift and thrust generation is observed owing to three-dimensional wing shape, trajectory, and vortex structure. Consequently, the results of the present work provide an important clue in understanding generation of aerodynamic force for rapid maneuverability in insects' flight.

Nomenclature

C_d	=	drag coefficient
C_l	=	lift coefficient
C_t	=	thrust coefficient, $-C_d$
c_m	=	mean chord length
f	=	flapping frequency, Hz
k	=	reduced frequency in terms of c_m, fc_m/U_m
Re	=	Reynolds number, $U_m c_m/\nu$
T	=	nondimensional flapping period
t	=	nondimensional time
U_m	=	mean wing velocity at aerodynamic mean chord
U_∞	=	freestream velocity
$x(t)$	=	lagging motion (horizontal direction motion)
$y(t)$	=	translation motion (vertical direction motion)
$\alpha(t)$	=	pitch angle motion
$\theta(t)$	=	elevation angle motion
ν	=	freestream kinematic viscosity
τ	=	pseudotime
$\phi(t)$	=	position angle motion

I. Introduction

INSECTS' flapping flight has been a subject of great interest to scientists and engineers working in many fields. This subject has been investigated from biological, biomechanical, morphological and aerodynamic perspectives. Especially, in the field of aeronautics, aerodynamics of insects' flapping flight have been considered as one of the most fascinating and challenging research subjects, because of its potential applicability to various propulsive devices or next generation aerospace vehicles. To understand its curious unsteady behavior, researchers have conducted experimental or computational studies on various flapping motions.

Experimental works on insects' wing motions have been carried out by Ellington et al. [1], Ward-Smith [2], Dickinson et al. [3,4], Yamamoto and Isogai [5], and so on. Ellington et al. [1] observed the leading-edge vortex (LEV) using smoke visualization around both a real moth and a three-dimensional model called "flapper" at the Reynolds number of $\mathcal{O}(10^3)$. They observed a strong vortex attached at leading-edge during downstroke motion. As another lift generation mechanism, vortical pattern produced by the "clap-fling" motion [2] was studied. Dickinson et al. [3,4] measured unsteady aerodynamic forces, and visualized flow patterns in an oil tank using a dynamically scaled mechanical model called "robofly." They observed two important lift enhancement mechanisms. The first one, called "rotational circulation," is analogous to the Magnus effect observed in rotating circular cylinder. The second one, called "wake capture," comes from the interaction between wing and shedding vortex by the wing rotation. Yamamoto and Isogai [5] measured unsteady aerodynamic forces of a mechanical flapping wing apparatus that dynamically simulates the tandem wing configuration of dragonfly, and investigated the flow interaction between the forewing and hindwing. Also, Okamoto and Azuma [6] performed experiments on combined heaving and feathering motions with various wing configurations, and examined unsteady aerodynamic characteristics at low-Reynolds number. Experimental works help explain global flow phenomena, but it is often difficult to describe detailed flowfields due to problems in modeling insects' wing motion and visualizing three-dimensional vortex structure.

Computational studies have been performed in parallel by several researchers. Sun and Yu [7] numerically simulated a two-dimensional clap-fling motion of a tiny insect using a NS solver, and showed that a sufficiently large amount of lift could be generated. Liu and Kawachi [8] verified the LEV of the moth (*manduca sexta*) wing under hovering flight by three-dimensional computation. Ramamurti and Sandberg [9] also performed three-dimensional computational study on the flapping wing of the modeled fruit fly. Lee et al. [10] designed an optimal flapping airfoil sustaining both high propulsive efficiency and thrust coefficient based on the understanding on the

Presented as Paper 2008-6400 at the 26th AIAA Applied Aerodynamics Conference, Honolulu, HI, 8–21 August 2008; received 5 February 2010; revision received 25 November 2010; accepted for publication 9 December 2010.

*Ph.D. Candidate, School of Mechanical and Aerospace Engineering. Student Member AIAA.

†Professor, School of Mechanical and Aerospace Engineering and Institute of Advanced Aerospace Technology; chongam@snu.ac.kr. Senior Member AIAA (Corresponding Author).

role of leading-edge and trailing-edge vortices. Furthermore, they explained the impulsive thrust generation mechanism of insects' forward flight by examining two-dimensional vortical flowfield [11]. Some review study on recent developments in flapping wing aerodynamics has been carried out by Platzer et al. [12] However, most of previous computational works have mainly focused on two-dimensional motion and/or hovering flight. Recently, unsteady aerodynamics of insects' forward flight have been studied by "three-dimensional" computational approaches, due to notable advances in modern computational fluid dynamics techniques and rapid growth of available computing power. Nagai et al. [13] conducted experimental and numerical simulations of a flapping wing of a bumblebee in forward flight. Unsteady aerodynamic forces and flow patterns around the flapping wing computed using a three-dimensional Navier–Stokes (NS) code. Ramamurti and Sandberg [14] performed three-dimensional unsteady computations of a maneuvering fruit fly, and investigated effect of kinematic difference between the right and left wings. Liu [15] developed a computational framework for modeling insect flapping flights, by integrating body—wing morphology, kinematics and unsteady aerodynamic NS solver. In addition, Young et al. [16] validated three-dimensional computations against smoke visualizations and digital particle image velocimetry measurements on real locusts, and analyzed the aerodynamic consequences of wing deformation on detailed wing kinematics. Other aspects of insects' hovering motion can also be found in the review papers [17,18].

Previous researches have pointed out that vortical pattern and interaction of vortices play a key role in generating unsteady aerodynamic forces and determining the propulsive efficiency of flapping motion. This suggests that detailed analysis on vortical structure is prerequisite to physical understanding on unsteady flapping flight. From this perspective, further study has to be carried out in the area of general flapping flight conditions. In particular, unsteady aerodynamic features on insects' forward flight and rapid maneuvering, based on detailed computations of complicated three-dimensional vortex structure, have not been addressed yet. Vortex generation, vortex–vortex and vortex–wing interaction around insects' wings play a crucial role in generating unsteady aerodynamic forces. Furthermore, wing–body interactions and wing flexibility are also important aspects to be incorporated for in-depth understanding on flapping wing aerodynamics. High-fidelity simulation and analysis are thus essential to unveil relevant flow physics.

Keeping these in mind, the present work focused on the unsteady flowfield characteristics around three-dimensional insects' flapping motion (or "figure-of-eight" motion) under forward flight condition. In the authors' preliminary research, two-dimensional results have shown very interesting and distinctive aerodynamic features, which could provide a decisive clue to understand three-dimensional counterpart. Such aerodynamic features can be summarized as "LEV generation due to a high effective angle of attack" and "vortex staying and vortex pairing phenomena" [11]. In particular, the impulsive thrust generation is closely related to vortex pairing in velocity field and vortex staying in pressure field, which is caused by the rotational component of figure-of-eight motion. To capture three-dimensional vortex structures, detailed three-dimensional wing simulation is conducted by using a realistic wing trajectory extracted from a blowfly's (*phormia regina*)s tethered flight experiment [19] under the freestream velocity of 2.75 m/s. Pressure field and vortical structure in the wake are examined to see whether the vortex staying and pairing, which has been observed in two-dimensional motion, can also be presented as a strong evidence for the impulsive large thrust generation. Other three-dimensional features, such as spanwise vortex, vortex ring, vortex pairing and wake structures, are investigated to identify characteristics of three-dimensional unsteady aerodynamic forces.

The present paper is organized as follows. After a brief review on two-dimensional study, numerical methods and modeling technique of three-dimensional flapping motion are introduced. After that, three-dimensional numerical investigations of figure-of-eight motion are carried. Finally, the role of vortex interaction and wake structure in generation of unsteady aerodynamic forces is examined.

II. Two-Dimensional Study

A. Numerical Modeling of Two-Dimensional Flapping Motion

Insects' flapping motion is mostly complex and fast. In two-dimensional side view, wing tip trajectory of many insects looks like the figure eight and this particular motion is used for hovering and forward flight. Nachtigall [19] examined the figure-of-eight motion from a tethered flight experiment. A blowfly was attached in the front of wind tunnel under a freestream velocity of 2.75 m/s, and wing kinematics was filmed using a high-speed camera. Figure 1 shows the corresponding wing tip trajectory. The wing motion consists of three components: translation ($y(t)$, vertical motion), lagging ($x(t)$, horizontal motion) and rotation ($\alpha(t)$). The wing translates relatively slowly during downstroke and its posture is approximately horizontal, and rotation is not severe. On the contrary, upstroke motion is fast and the leading edge is sharply pitched up. Especially, the rapid wing rotation is mainly concentrated near the end of upstroke. Detailed numerical modeling including flow condition and geometric modeling can be found in [11].

B. Aerodynamic Features of Two-Dimensional Flapping Motion

From Figs. 2 and 3, lift is mainly generated during downstroke motion, while thrust is impulsively produced at the end of upstroke. Figure 4 shows pressure and velocity vector fields at $t = 8.1T$ (T: nondimensional flapping period) and $8.4T$, when the instantaneous lift coefficient reaches the local maximum value. It is clearly seen that the location of the LEV center (the left figure) and the location of pressure suction peak (the right figure) on the wall are almost the same. The instantaneous lift enhancement comes from the lower pressure distribution induced by the LEV. The stroke path of the insect wing in normal hovering is almost horizontal, but it maintains a high geometric angle of attack to produce a strong LEV [4,20]. In case of forward flight, development of the LEV and the lift

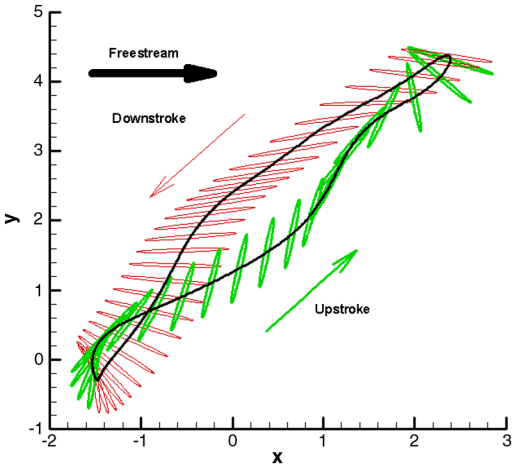

Fig. 1 Nondimensional position of a blowfly's wing element during tethered flight: downstroke phase and upstroke phase.

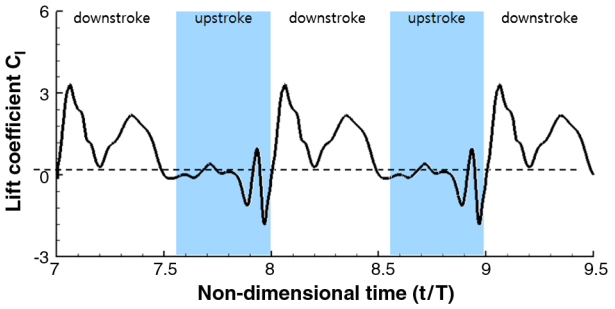

Fig. 2 History of instantaneous lift coefficient (two-dimensional figure-of-eight motion).

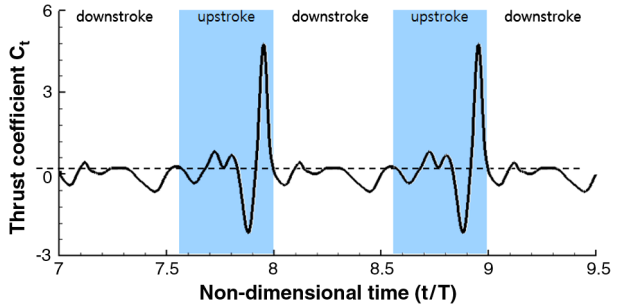

Fig. 3 History of instantaneous thrust coefficient (two-dimensional figure-of-eight motion).

enhancement appear at low or even at negative geometric angle of attack (Fig. 4). This is because the LEV in forward fight is produced by an effective angle of attack rather than a geometric angle of attack. From the aerodynamic point of view, this is quite understandable. If the wing maintains a high geometric angle of attack, a substantial amount of drag would be created by the LEV which makes the forward flight almost impossible or very inefficient.

Vorticity and pressure fields are examined to understand aerodynamic mechanism of the impulsive thrust generation in Fig. 3. Figure 5a shows pressure and velocity distribution at $t = 8.95T$ when thrust becomes maximal. A clockwise vortex is developed from the shear layer of trailing edge. Velocity field indicates rapid flow acceleration at lower surface of airfoil. Flow around leading and trailing edges is being sucked into the airfoil. As a result, a wide low-pressure region is developed while pressure at the upper surface is relatively high. Thrust is then created due to the "vortex staying" phenomenon. Figure 5b is velocity and vorticity fields in the wake region at the end of upstroke. The two trailing-edge vortices vertically align and a strong jet is induced, which contributes to the impulsive thrust generation.

In summary, the two-dimensional analysis provides the basic understanding on vortex and flow patterns in terms of "LEV generation due to a high effective angle of attack" and "vortex staying and vortex pairing phenomena" [11]. The corresponding flow physics for three-dimensional motion has to be resolved.

III. Numerical Methods

A. Governing Equations

The flowfield around the blowfly wing is low-Reynolds-number flow, and the governing equations are the three-dimensional unsteady incompressible NS equations:

$$\frac{\partial \mathbf{v}}{\partial t} + \mathbf{v} \cdot \nabla \mathbf{v} + \nabla p = \nabla \cdot \sigma \tag{1}$$

$$\nabla \cdot \mathbf{v} = 0 \tag{2}$$

where p denotes the pressure, and $\mathbf{v} = \mathbf{v}_a + \mathbf{w}$ is the flow velocity. Here, $\mathbf{v}_a$ is the convection velocity, and $\mathbf{w}$ is the mesh velocity to present the figure-of-eight motion, and σ is the stress tensor. Both pressure and stress tensor are normalized by density. The artificial-compressibility method is employed to satisfy the momentum Eq. (1) by iteratively updating velocity and pressure fields:

$$\frac{\partial p}{\partial \tau} = -\beta \nabla \cdot \mathbf{v} \tag{3}$$

The upwind-biased Osher's flux difference splitting is used for spatial discretization [21]. A third-order variable reconstruction is

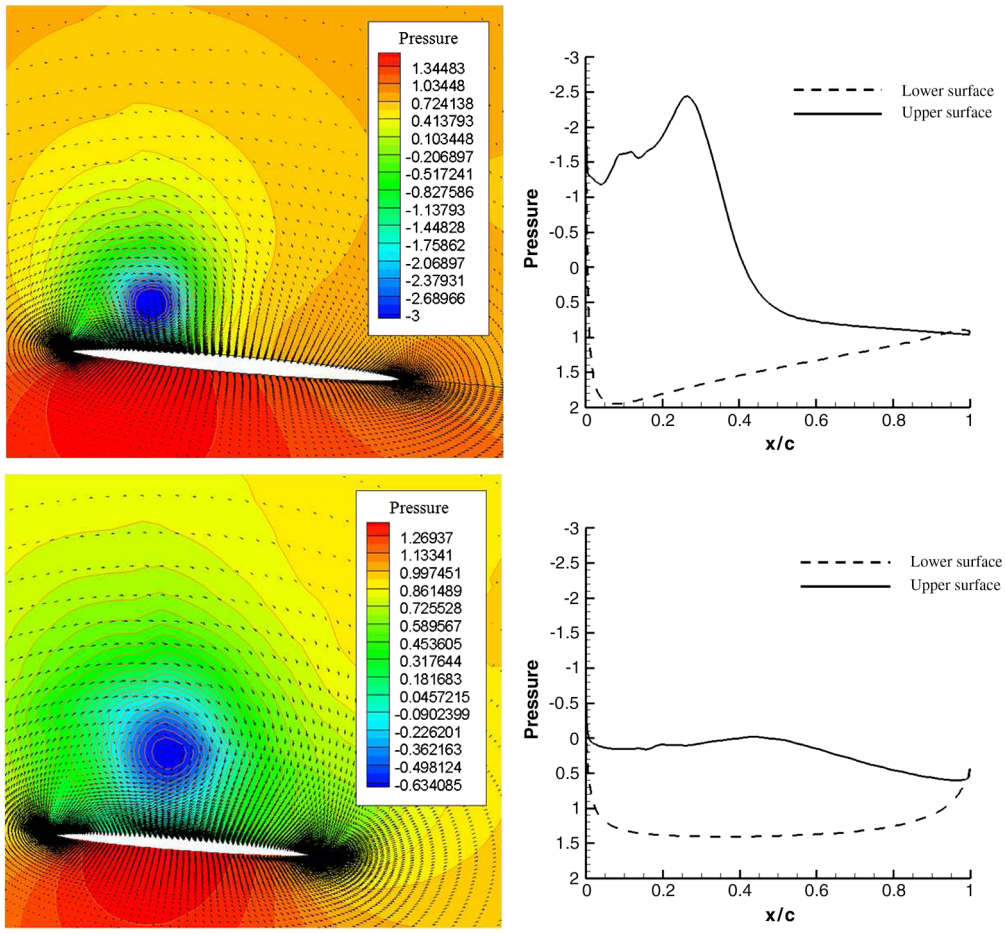

Fig. 4 Two-dimensional leading-edge vortex at $t = 8.1T$ (top) and $8.4T$ (bottom): pressure and velocity vector field (left) and pressure distribution on the wall (right).

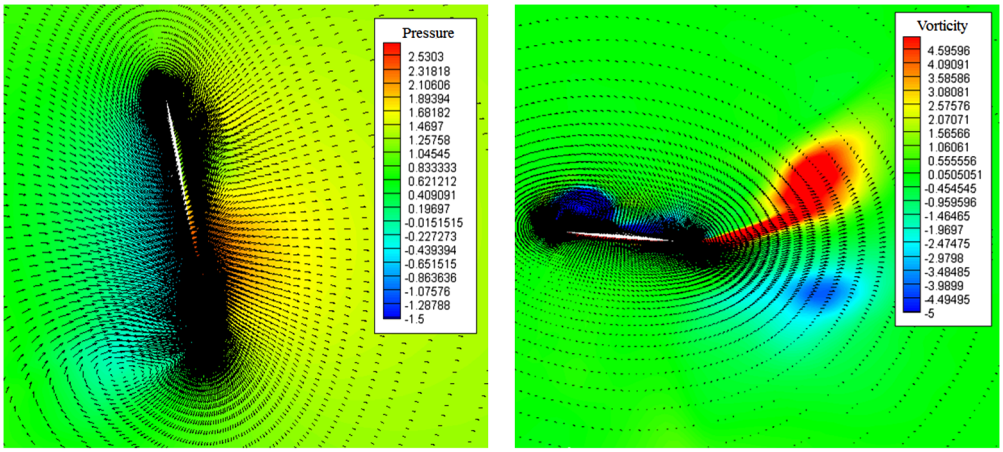

a) b)

Fig. 5 Vortex staying (left) and vortex pairing (right) in two-dimensional motion.

employed to attain a higher-order spatial accuracy. For time integration, lower upper symmetric Gauss–Seidel scheme is used together with the dual time stepping method. The final discretized form of the governing equations can be written as

$$\left[\frac{I}{J\Delta\tau}+\left(\frac{\partial\hat{R}}{\partial Q}+\frac{\partial\hat{S}}{\partial Q}\right)^{n+1,m}\right]\Delta Q^{n+1,m}=-(\hat{R}^{n+1,m}+\hat{S}^{n+1,m}) \quad (4)$$

Superscript n indicates the physical time level, and m denotes the pseudotime iteration. $\hat{R}$ is the residual vector including inviscid and viscous fluxes, $\hat{S}$ is an unsteady sourcelike term, Q is the flow variable vector, and J is the flux Jacobian. Detailed numerical procedure can be found in [21,22].

B. Kinematic Modeling

Several researchers have measured wing trajectories using wind tunnel and high-speed camera system. Nachtigall [19] suspended a blowfly in front of an open wind tunnel, and adjusted wind speed until the net horizontal force acting on the blowfly is zero to realize a forward flight condition. Figure 6 depicts a measuring technique of wing kinematics. The trajectory of the wing tip can be uniquely described by the three angles (β, γ, δ) projected onto three mutually perpendicular planes (yz, xy and zx planes). The two-dimensional side-view of many insects looks like the figure eight, and the figure-of-eight motion was first observed by the French physiologist Marey in 1869 [4,23]. Figure 7 shows the trajectories of the three angles $(\beta(t), \gamma(t), \delta(t))$ during two and a half successive wing beats. They are measured clockwise from the positive x, z and negative y direction, respectively (see Figs. 6 and 7).

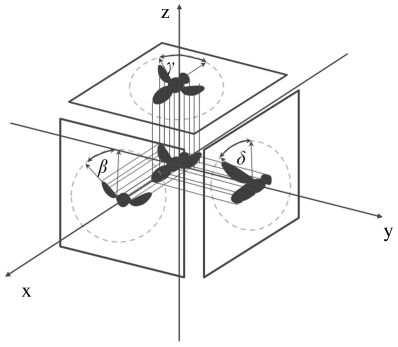

Fig. 6 Projection of a flying insect onto three perpendicular planes (xy, yz, zx).

To reproduce the blowfly's three-dimensional wing motion in computational coordinate, it is convenient to use pitch angle ($\alpha(t)$, see Fig. 1) as well as $(\beta(t), \gamma(t), \delta(t))$. Note that $\delta(t)$ is different from $\alpha(t)$. Figure 8 explains a sequence of rotation adopted in computational coordinate. A rotation with respect to the y axis ($\alpha(t)$, pitch angle) is first applied, then to the z axis ($\phi(t)$, position angle) and finally to the x axis ($\theta(t)$, elevation angle). $\alpha(t)$ is obtained from experiment, and $(\phi(t), \theta(t))$ can be determined from $(\beta(t), \gamma(t))$ through the geometric relationship as explained in Figs. 8 and 9. After rotating pitch and position angle (Figs. 8a and 8b), the top view of the wing is shown in Fig. 9a. The wing is then rotated with elevation angle (Fig. 8c) and the back view looks like Fig. 9b. However, before and after the rotation of elevation angle, the top view changes as seen in Fig. 9c. Thus, position angle $\phi(t)$ has to be corrected by considering the angle change induced by the rotation of elevation angle. $\phi(t)$ is then obtained from $(\beta(t), \gamma(t))$ as follows:

$$\tan\gamma=\frac{P}{d} \quad (5)$$

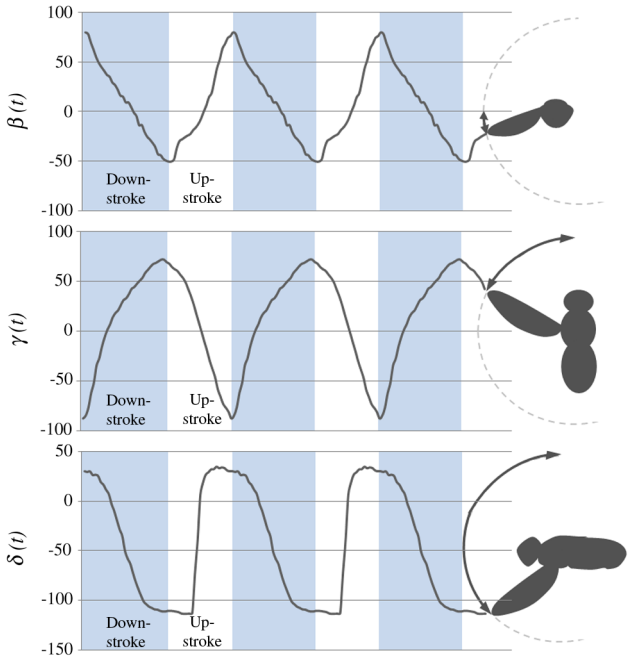

Fig. 7 Time history of three angles (β, γ, δ) as a function of wing beat [19].

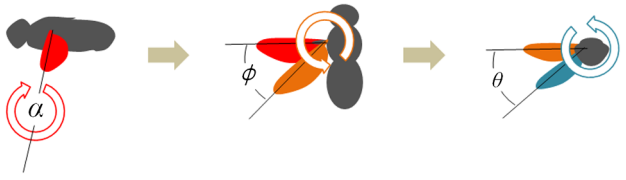

a) b) c)

Fig. 8 Transformation of insect wing motion: a) pitch angle rotation, b) position angle rotation, and c) elevation angle rotation.

$$P = R\sin\phi, \qquad b = R\cos\phi, \qquad d = b\cos\beta = R\cos\phi\cdot\cos\beta \tag{6}$$

$$\tan\gamma = \frac{P}{d} = \frac{R\sin\phi}{R\cos\phi\cdot\cos\beta} = \frac{\tan\phi}{\cos\beta} \tag{7}$$

$$\phi = \tan^{-1}(\tan\gamma\cdot\cos\beta) \tag{8}$$

From Fig. 9b, $\theta(t)$ is the same as $\beta(t)$. Finally, $(\alpha(t), \phi(t), \theta(t))$ can be expressed using Fourier series with the Fourier coefficients of a_0, a_n and b_n:

$$\begin{aligned}
\alpha(t) &= a_0 + \sum_{n=1}^{m}(a_n\cos(2\pi nkt) + b_n\sin(2\pi nkt))\\
\phi(t) &= a_0 + \sum_{n=1}^{m}(a_n\cos(2\pi nkt) + b_n\sin(2\pi nkt))\\
\theta(t) &= a_0 + \sum_{n=1}^{m}(a_n\cos(2\pi nkt) + b_n\sin(2\pi nkt))
\end{aligned} \tag{9}$$

The insect wing relative to the insect body (or wing root) in computational coordinate (see Fig. 10b) can be rotated sequentially: the pitch angle (α) with respect to the y axis, the position angle ϕ to the z axis, and the elevation angle θ to the x axis, which can be expressed in a matrix form:

$$\begin{aligned}
\text{Pitch:}\quad &\begin{bmatrix} x_\alpha \\ y_\alpha \\ z_\alpha \end{bmatrix} = \begin{bmatrix} \cos\alpha & 0 & \sin\alpha \\ 0 & 1 & 0 \\ -\sin\alpha & 0 & \cos\alpha \end{bmatrix}\begin{bmatrix} x_0 \\ y_0 \\ z_0 \end{bmatrix}\\
\text{Position:}\quad &\begin{bmatrix} x_{\alpha\phi} \\ y_{\alpha\phi} \\ z_{\alpha\phi} \end{bmatrix} = \begin{bmatrix} \cos\phi & \sin\phi & 0 \\ -\sin\phi & \cos\phi & 0 \\ 0 & 0 & 1 \end{bmatrix}\begin{bmatrix} x_\alpha \\ y_\alpha \\ z_\alpha \end{bmatrix}\\
\text{Elevation:}\quad &\begin{bmatrix} x_{\alpha\phi\theta} \\ y_{\alpha\phi\theta} \\ z_{\alpha\phi\theta} \end{bmatrix} = \begin{bmatrix} 1 & 0 & 0 \\ 0 & \cos\theta & \sin\theta \\ 0 & -\sin\theta & \cos\theta \end{bmatrix}\begin{bmatrix} x_{\alpha\phi} \\ y_{\alpha\phi} \\ z_{\alpha\phi} \end{bmatrix}
\end{aligned} \tag{10}$$

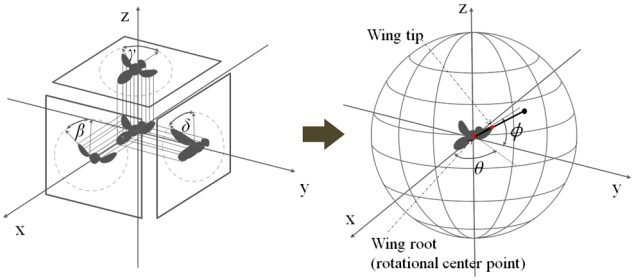

a) b)

Fig. 10 Coordinate transformation: a) experimental coordinate system and b) computational coordinate system.

C. Geometric Modeling and Boundary Condition

For geometric modeling of wing shape, the picture of the blowfly's wing is scanned from [19], and the wing root region is restored and simplified as shown in Fig. 11a. A 225×97 grid is used for the sectional surface of the modified wing (see Fig. 11b). For the sake of simplicity, wing sectional shape is assumed to be a very thin flat plate with 5% thickness of mean chord length. As shown in Fig. 12, whole mesh system is composed of six blocks, and two sets of mesh systems are considered: 3.1 and 6.2 million, respectively. Wall spacing is 5×10^{-4} chord, and outer boundary of the computational domain extends to 25 chords (or, equivalently, 10 times the wing span).

Inflow and outflow boundary conditions are based on the method of characteristics. For inflow, velocity component is specified from the freestream condition, and pressure is extrapolated from interior grid points. For outflow, pressure is specified and velocity component is determined by extrapolation. Velocity component is an approximate Riemann invariant corresponding to the characteristic wave. Symmetric condition is imposed on the symmetry boundary (the wing root plane or the plane of $y = 0$, Fig. 13b). The whole mesh system rotates according to kinematic modeling data, and the rotated computational mesh is divided by the symmetry plane (the plane of $y = 0$, Fig. 13c). The left hemisphere (or the left computational domain) is then treated as a hole region as in overset grid system. Physical variables on the symmetry plane are interpolated from nearest available data in the right hemisphere (or actual computational domain, Fig. 13c).

The Reynolds number in this work is low ($Re = \mathcal{O}(10^3)$), and all computations have been conducted under laminar flow assumption. Standard parallel computing technique using message passing interface programming has been implemented.

D. Code Validation

To validate the present numerical approach, computations have been carried out for a fruit fly under the conditions described in [24,25]. Figure 14a shows a six-block and 3.1 million grid points of mesh system used for the geometric modeling of the insect wing. Figure 14b shows flapping wing trajectory of the fruit fly in [24,25]. Reynolds number is 134, and reduced frequency (k) is 0.212. More details on flow conditions can be found in [25]. Figure 15 shows the time histories of vertical and horizontal forces. Computed results are compared with other computations from Aono et al. [25] and experimental data of Fry et al. [24]. As in Figs. 15a and 15b, the

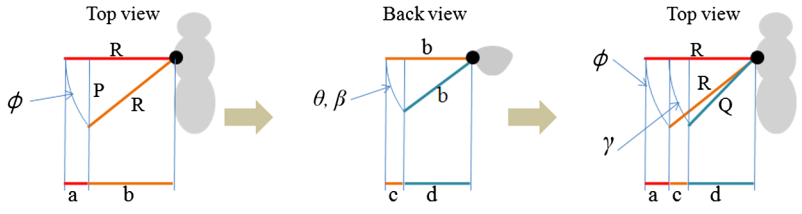

a) b) c)

Fig. 9 Correction of rotation angle: a) position angle rotation, b) elevation angle rotation, and c) relation between position angle and projected angle in xy plane γ.

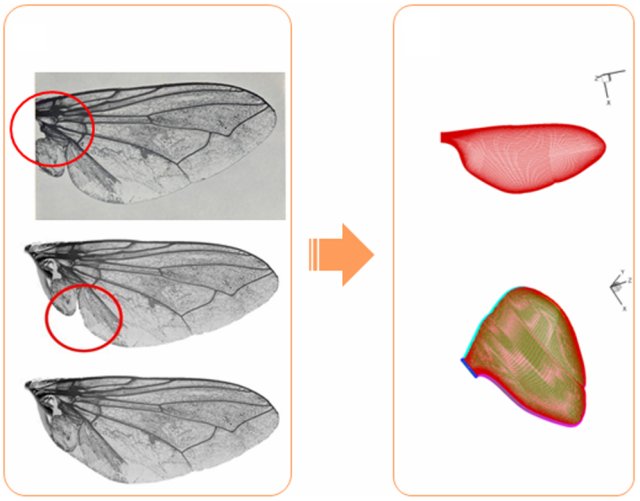

a) b)

Fig. 11 Geometric modeling: a) tailoring of a blowfly's wing shape (circle: restored and simplified part of wing surface) and b) final wing surface grid.

present results are similar to other computations and show a reasonable agreement with the experimental data. The difference seems to be caused by an imperfect match between computational modeling and experimental condition.

IV. Numerical Results

Verification study has been performed in term of grid refinement and time step sensitivity. For the blowfly's forward flight, two sets of mesh systems are considered: 3.1 and 6.2 million grid points. Computational comparison shows overall aerodynamic characteristics are almost the same and only a slight difference is observed. As shown in Figs. 16a and 16b, the maximum difference for the lift and thrust coefficients between the two cases is less than 5% but it is less than 0.1% in most regions. The effect of time step size on aerodynamic force generation is examined using three different time steps ($1/500T$, $1/1000T$, and $1/1500T$). As in Figs. 16c and 16d, the results are very insensitive to time step change. Based on the verification results, 6.2 million grid system and the physical time step of $1/1000T$ are used for accurate computations.

There are several ways to define the Reynolds number of insects' flapping motion [23]. The Reynolds number in the present work is defined by using the mean velocity of the wing motion:

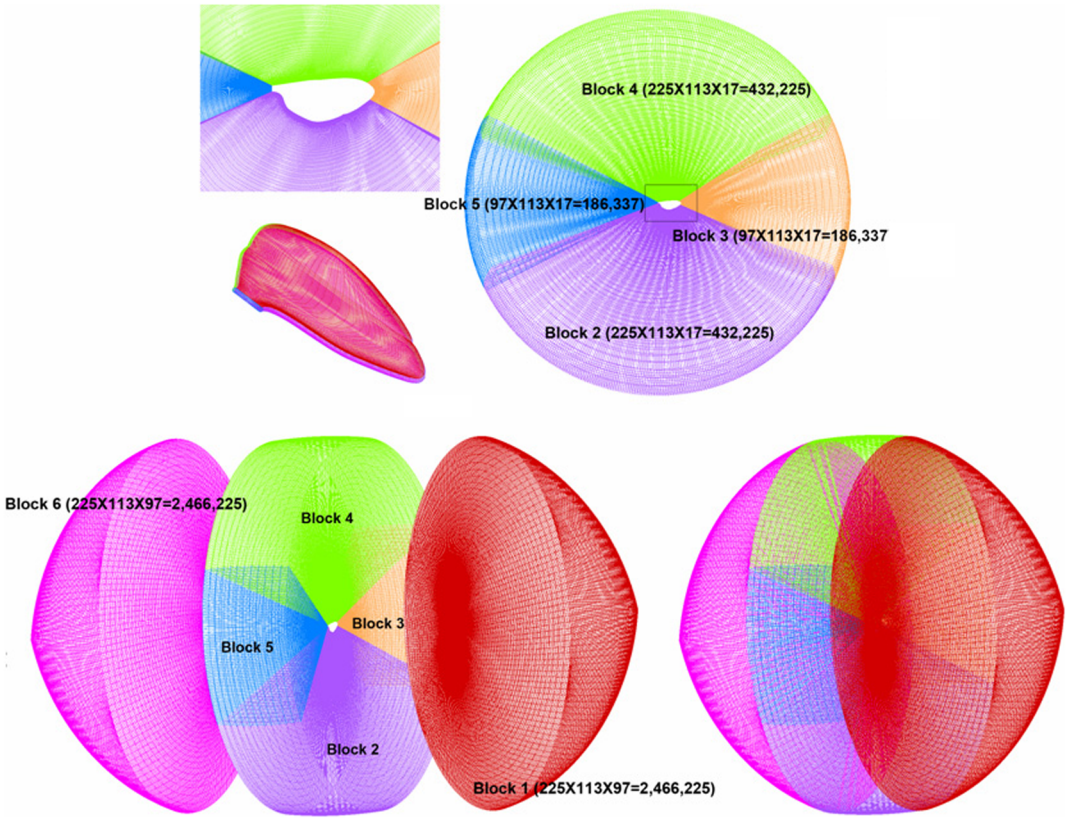

Fig. 12 Multiblock grid system.

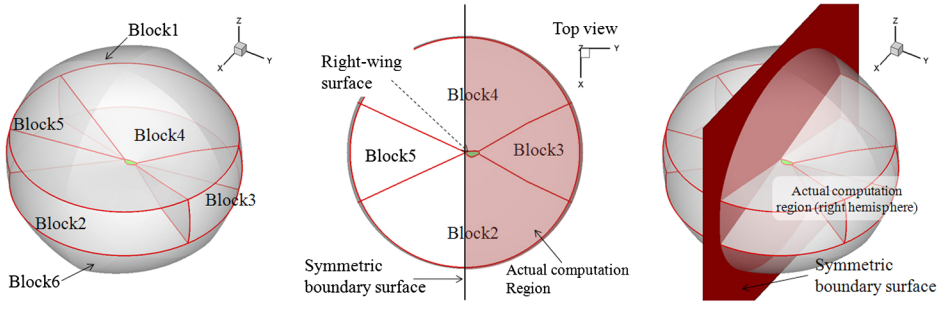

a) b) c)

Fig. 13 Symmetric boundary condition: a) whole grid system, b) symmetric boundary surface, and c) actual computation region.

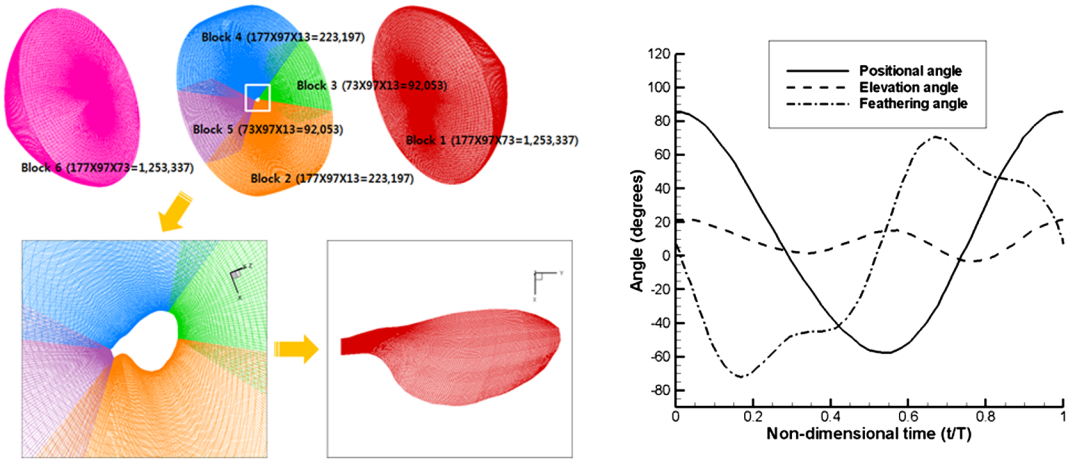

a) b)

Fig. 14 Geometric and kinematic modeling of fruit fly: a) six-block and 3.1 million grid points of mesh system and b) flapping wing trajectory of fruit fly obtained from [24,25].

$$Re = \frac{U_m c_m}{\upsilon} \tag{11}$$

where U_m is defined at aerodynamic mean chord, and c_m is the mean chord length.

Based on two-dimensional results [11], computation is carried out up to seven cycles to obtain sufficiently periodic behavior of aerodynamic coefficients. Physical time step is obtained by dividing one cycle into 1000 subintervals ($1/1000T$). At each physical time step, pseudoiteration is carried out until both the maximum divergence of velocity and the maximum residual are less than 1×10^{-5}. Figure 17 shows the directions of aerodynamic force (positive z: lift, negative x: thrust) and freestream. As in wind-tunnel experiment, the direction of thrust and lift is defined with respect to the direction of the insect's body. Table 1 shows flow conditions including nondimensional parameters for numerical computations in Nachtigall's [19] experimental data.

A. Definition of Vortex Structure

Several vortex structures are first defined to conveniently describe the flowfield. As in Fig. 18, vortex structure could be classified into two groups. The first one is the vortex structure caused by translational motion normal to wing surface, which is named translation motion vortex (TMV). TMV structure is further divided into two types: perfect vortex tube (PVT) and "perfect" vortex ring (PVR). Here, *perfect* indicates that the direction of vortex tube or ring is not reversed. As depicted in Fig. 18, when the LEV or the trailing-edge vortex (TEV) is combined with the wing tip vortex (WTV), the resulting vortex structure looks like a tube. When the three vortices (LEV, WTV, and TEV) in the same direction are completely merged into a single "ring," PVR is formed. Studies on vortex structure and the related unsteady aerodynamics have been conducted in hovering flight. Depending on the growth and evolution of initial vortex ring, Aono et al. [25] defined horseshoe-shaped vortex (HSV) and doughnut-shaped vortex ring. Later, Liu et al. [15,26] described the same vortex structure with the downstroke vortex tube ring and the upstroke vortex tube ring to investigate the role of the vortex ring in stabilizing the LEV. Here, the TMV or PVR are similar to the HSV and doughnut-shaped vortex ring, in a sense that the HSV and doughnut-shaped vortex ring are developed along the wing edge in the early down- and upstroke.

The other one is the vortex structure caused by rotational motion with respect to wing surface, which is named as rotation motion vortex (RMV). This vortex structure is observed mostly in insect' forward flight condition. In this case, only a single RMV structure is observed: "imperfect" vortex ring (IPVR). An IPVR is composed of the same three vortices (LEV, WTV, and TEV), but the direction of LEV is opposite to that of TEV. Depending on rotational phase, WTV is combined with LEV or TEV. LEV and TEV of IPVR are not directly connected with each other but formed a ring shape together with WTV.

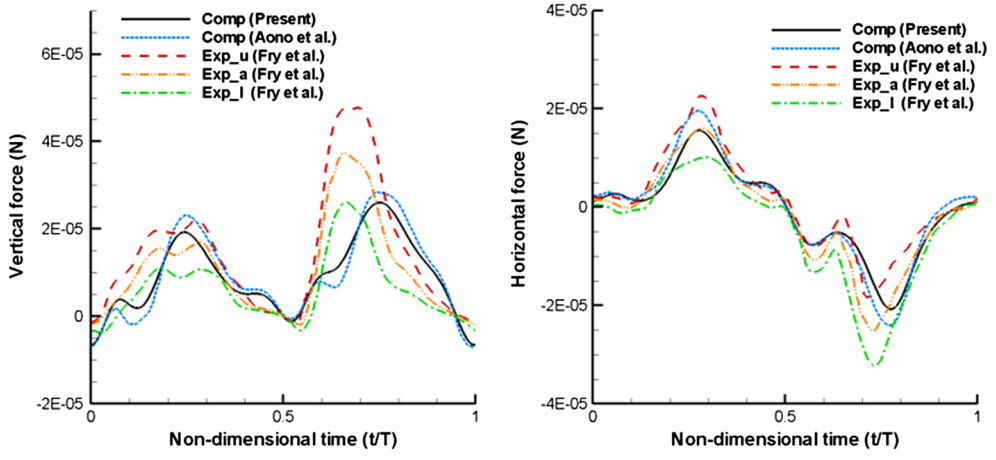

a) b)

Fig. 15 Time histories of the a) vertical and b) horizontal forces: solid line, computed result (present); dotted line, computed result (Aono et al. [25]); dashed line, upper values of experiment (Exp_u, Fry et al. [24]); dash–dot–dot line, average values of experiment (Exp_a); and dash–dot line, lower values of experiment (Exp_l).

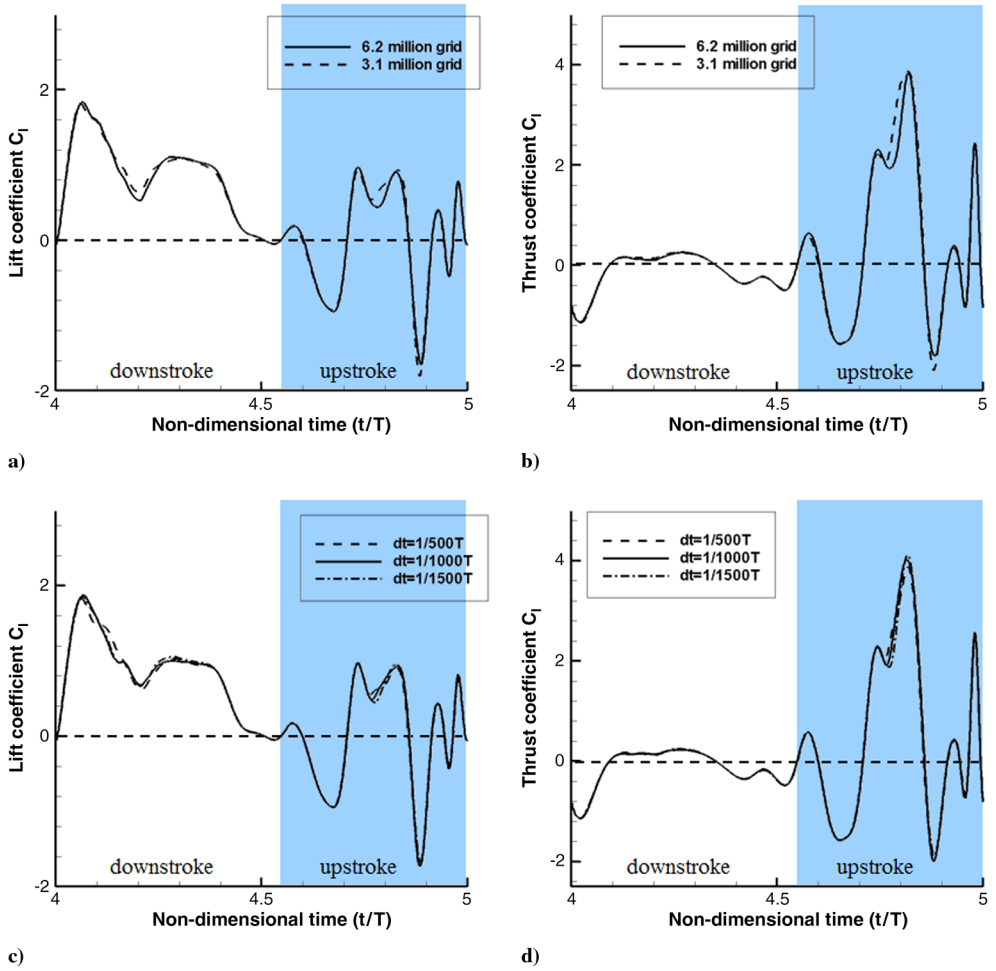

Fig. 16 Grid refinement and time step sensitivity: a–b) grid refinement test with two sets of mesh systems and c–d) time step sensitivity test using three time steps.

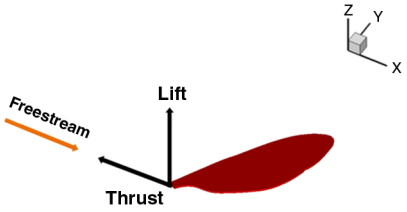

Fig. 17 Direction of aerodynamic force.

B. Overall Flow Features

Figures 19 and 20 show temporal histories of instantaneous lift and thrust coefficients. Local behavior is clearly different from the two-dimensional result, but the main flow physics is somewhat similar: lift is mainly generated during downstroke, while thrust is impulsively produced at some location of upstroke (see Fig. 3). Based on the two-dimensional study [11], similar analysis is carried out to understand the role of vortex structure and vortex interaction in three-dimensional lift and thrust generation.

1. Downstroke

Figure 21 shows sequential snapshots of vorticity, cross-sectional pressure distribution in the spanwise direction at $r/R = 0.2, 0.5, 0.8$, and surface pressure distributions, respectively.

At early downstroke, a strong vortex ring (PVR) resulting from the impulsive rotational motion at the end of upstroke stays on the upper surface, and it produces a low-pressure region (Fig. 21a). Afterwards, the wing tip portion of the PVR begins to detach from the upper surface due to the lack of the spanwise flow component (Fig. 21b), and eventually only the LEV part of the PVR stays on the wing surface (Figs. 21d and 21e). At the same time, however, a vortex tube is newly developed at the detached wing tip region, and it is gradually connected to the LEV to form a combined PVT (Fig. 21c), and it maintains a low-pressure region along leading edge of the upper surface (Figs. 21d and 21e). Finally, as the wing continuously translates downward, the combined vortex tube (PVT) at leading edge completely sheds from the wing (Fig. 21f).

In two-dimensional case, the LEV periodically sheds into the wake [11], and the corresponding lift history is severely fluctuating (Fig. 2). In three-dimensional case, the LEV does not immediately shed into the wake due to the spanwise flow component, which prevents the buildup of vorticity at leading edge and thus delays separation of the LEV. As a result, the lift history is much less fluctuating than the two-dimensional motion (Fig. 19).

2. Upstroke

Figure 3 shows that lift generation is mild but thrust is impulsively generated at the end of upstroke in two-dimensional case. On the

Table 1 Flapping motion data [19] and nondimensional parameters

Parameter	Symbol	Value
Airspeed	U_∞	2.75 m/s
Mean wing velocity	U_m	5.79 m/s
Chord length	c_m	3.8 mm
Reynolds number	Re	1466.8
Flapping frequency	F	130.6 Hz
Reduced frequency	K	0.0857
Stroke plane angle	β	45°
Body angle	χ	0°

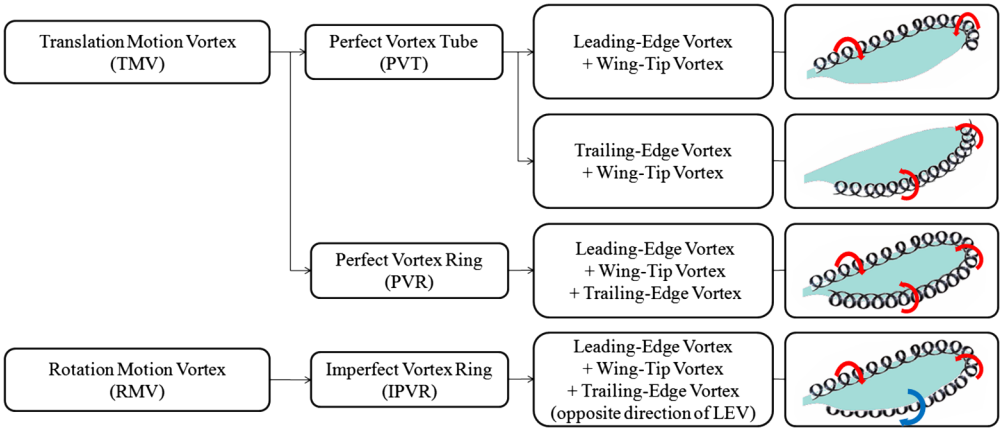

Fig. 18 Definition of vortex structure.

other hand, lift and thrust pattern in three-dimensional motion is substantially different as shown in Fig. 20. Figure 22 shows three-dimensional vorticity magnitude and surface pressure distributions around the middle of upstroke. At an early upstroke, wing rotation induces a low-pressure region on the upper surface and a high-pressure region on the lower surface, which produces negative lift and thrust (Figs. 19, 20, and 22a). The insect's wing is then moving toward the top location of the figure-of-eight trajectory (Figs. 22b–22d). Noticeable amount of lift is generated and, in particular, multiple thrust peaks are observed at the middle and end of upstroke. This is quite different from two-dimensional result. All of the aerodynamic differences can be explained by three-dimensional effects of insects' wing motion. In two-dimensional case, the two-dimensional wing, which is simply the mean chord at 60% of the wing root, moves with very high (almost vertical) angle of attack at the middle of upstroke (see Fig. 1). As a result, lift cannot be large, and net thrust force is small: thrust force acting on the upper surface owing to the retreating motion of the two-dimensional wing, and drag force acting on the lower surface due to freestream are somewhat balanced. In three-dimensional case, however, substantial amount of lift and thrust is generated at the middle of upstroke (Figs. 19 and 20).

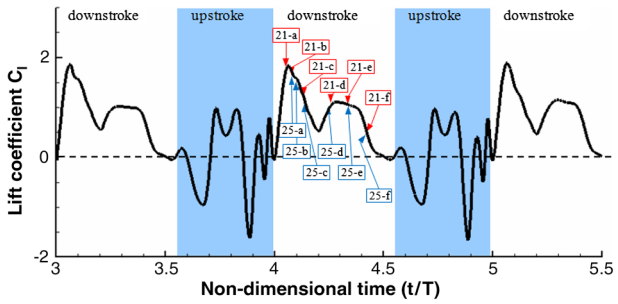

Fig. 19 Time history of instantaneous lift coefficient in three-dimensional figure-of-eight motion.

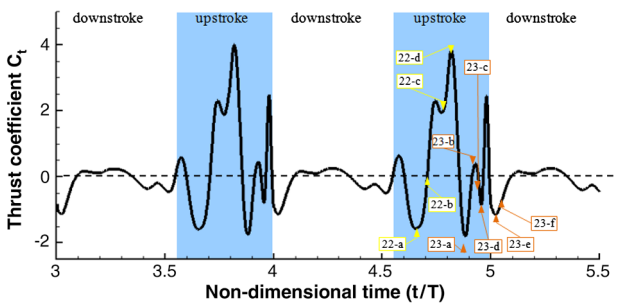

Fig. 20 Time history of instantaneous thrust coefficient in three-dimensional figure-of-eight motion.

Owing to three-dimensional geometric configuration and kinematics, the resultant force acting on the two-dimensional wing section is not parallel to the flight direction but changing along the spanwise direction. Thus the net lift and thrust is different from the two-dimensional counterpart. In particular, the wing produces a large amount of thrust at the middle of stroke. When the insect's wing performs flapping motion, wing velocity is linearly increasing from wing root to wing tip due to wing rotation, and the resultant force acting on the wing surface is squarely increasing. In the inner region (near wing root region) of the wing, the two opposite forces (thrust force acting on the upper surface, and drag force acting on the lower surface) are roughly balanced and thus produce little net force. In the outer region (near wing tip region) of the wing, wing velocity is high enough, and the pressure difference between the upper and lower surface becomes large. As a result, the wing generates sizable lift and thrust forces at the middle of upstroke. The surface pressure distribution in Figs. 22c and 22d clearly supports this observation.

Figure 23 shows three-dimensional vorticity magnitude, cross-sectional pressure field in the spanwise direction at $r/R = 0.2$, 0.5, 0.8, and surface pressure distributions at the end of upstroke. Similar to the two-dimensional results, as the wing starts to rotate counterclockwise and translate upward (Fig. 23a), a LEV is developed in the upper surface. As the wing continuously rotates, the LEV is strengthened and a TEV is generated in the lower surface (Figs. 23b and 23c), and finally the two vortices (LEV and TEV) form an IPVR together with a WTV, along the path from the upper leading edge, wing tip to the lower trailing edge (Fig. 23c). At the same time, due to the translational motion, the LEV gradually slides away from the upper leading edge, and the TEV moves toward the lower leading edge. However, it is observed that the IPVR is still maintained and the TEV part of the IPVR stays for a while near the lower surface (Fig. 23d). Thus, low-pressure region is developed on the lower surface, which promotes thrust force. This is the three-dimensional vortex staying phenomenon, which was originally observed in two-dimensional motion [11], where a two-dimensional TEV completely sheds from the two-dimensional wing but the detached two-dimensional TEV stays for a while at the same position (Fig. 5a). At the end of upstroke, a new TEV is generated in the opposite direction of the detached TEV of the IPVR (Fig. 23e). Finally, the two vortices (the detached clockwise TEV of the IPVR and the newly formed counterclockwise TEV) form a pairing and move into the downstream (Fig. 23f). This the three-dimensional vortex pairing phenomenon observed in two-dimensional motion [11], which is responsible for an impulsive thrust at the end of upstroke (Figs. 3 and 5b). This will be examined again in Sec. IV.C.

C. Flowfield Characteristics

In Sec. IV.B, computed flowfields were examined in terms of down- and upstroke motion. It was observed that vortex structure is a crucial factor in determining unsteady aerodynamic characteristics of three-dimensional flapping motion. This section is thus devoted in examining various vortex structures in detail.

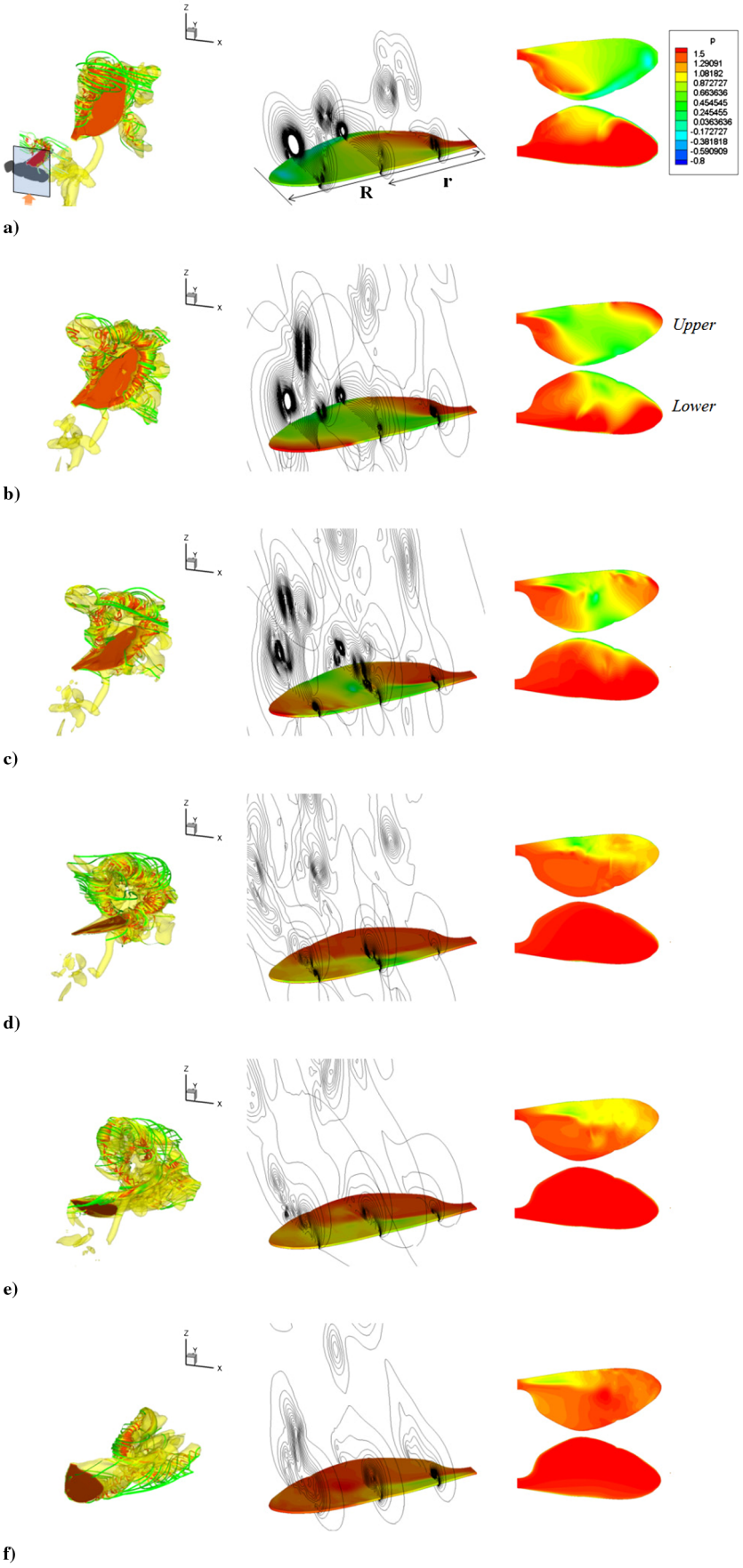

Fig. 21 Vorticity (left), cross-sectional pressure field (middle), and surface pressure (right) during downstroke: a) $t = 4.05T$, b) $t = 4.08T$, c) $t = 4.13T$, d) $t = 4.26T$, e) $t = 4.34T$, and f) $t = 4.42T$.

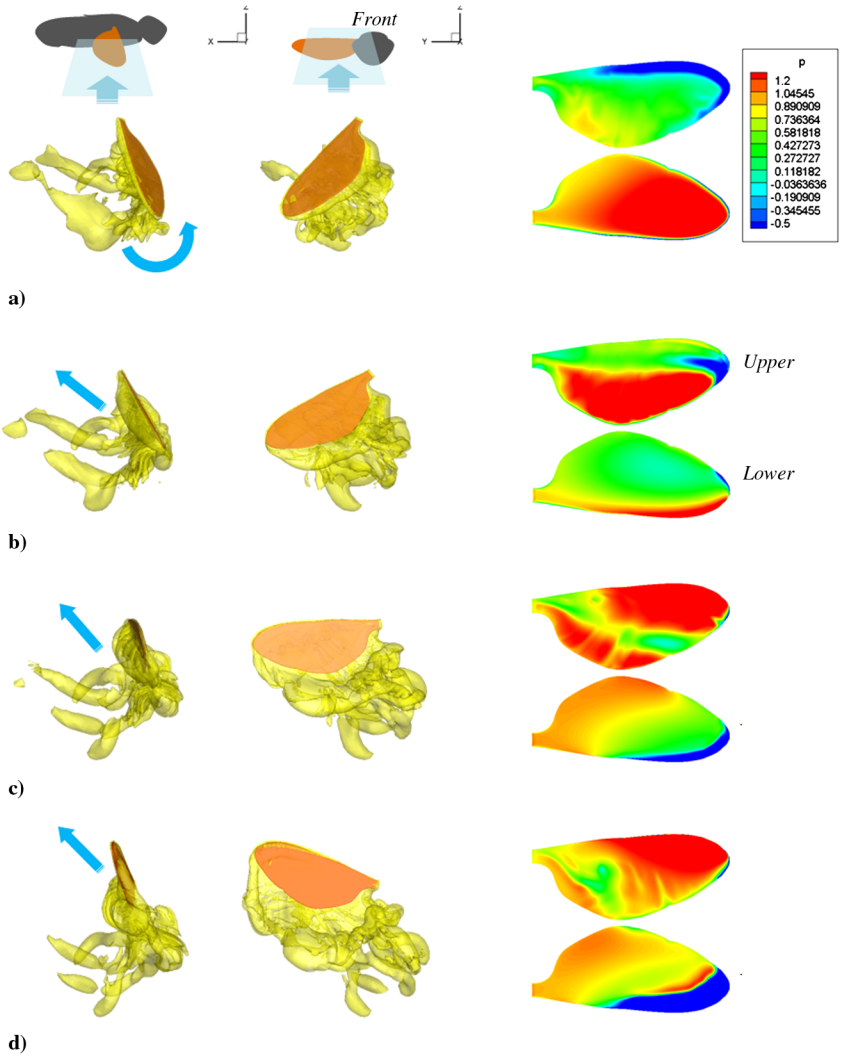

Fig. 22 Vorticity (left, middle) and surface pressure (right) during middle upstroke: a) $t = 4.66T$, b) $t = 4.71T$, c) $t = 4.77T$, and d) $t = 4.82T$.

1. Spanwise Flow and Vortex

The most conspicuous feature of three-dimensional flapping motion is the existence of spanwise flow and the delayed stall. Through experimental and computational studies, existence of the spanwise vortex and its effects has been reported [4,8,9,27,28]. Figure 24 shows a flow structure including the spanwise flow component and LEV. The spanwise flow delays the separation of the LEV, and thus the lift coefficient during downstroke is much less fluctuating than two-dimensional case (Figs. 2 and 19). Figure 25 shows the attachment and detachment of the LEV and WTV during downstroke. In Figs. 25a–25c, the flowfield covered by the LEV is gradually expanded owing to the spanwise flow component. The LEV is then combined with a newly generated WTV to form a PVT. As a result, the low-pressure region around leading edge is expanded (Fig. 25c), and a substantial amount of lift is generated. This is the physical reason why three-dimensional flapping motion is less fluctuating. The vortex shedding pattern observed in two-dimensional analysis does not happen. Instead, part of the PVT around wing tip region ($r/R = 0.0 \sim 1.0$) is eventually separated from the PVT due to the rapid motion normal to the wing surface, while part of the PVT around wing root region ($r/R = 0 \sim 0.5$) is steadily attached to leading edge (Figs. 25d–25f). This comes from the momentum balance between the rapid wing motion and the spanwise flow. These observations are consistent with experimental and computational results in [8,28], in which the role of spanwise flow and LEV in lift generation is explored for hovering case. It has also been reported in [8,28] that LEV with the spanwise flow breaks down at about 50% wing length. Similar to hovering flight, the spanwise flow and characteristic of the partially attached LEV play a key role in generating and sustaining lift in forward flight motion.

2. Vortex Ring

Figure 26 describes two distinct formations of vortex ring (or vortex tube) observed in three-dimensional flapping motion. A PVR is developed when translational motion normal to the wing surface is dominant, as in downstroke motion. Because the unidirectional spanwise flow component, LEV, WTV and TEV are fully coupled and formed a perfect vortex ring. Here, *perfect* means the direction of the three vortices (LEV, TEV, and WTV) is the same and they form a complete vortex ring. The PVR is responsible for lift generation during downstroke. On the contrary, an IPVR is developed when rotational motion is dominant. When the wing rotates, the directions of leading-edge and trailing-edge vortices are opposite. At the same time, the wing experiences an upward or downward translation motion in down- or upstroke motion. Only LEV and WTV (or TEV and WTV) are directly combined, and the remaining vortex is just loosely coupled to form a ring shape along the path from the upper leading edge, wing tip to the lower trailing edge. The TEV of the IPVR takes part in three-dimensional vortex staying and vortex pairing phenomena for thrust generation at the end of upstroke. In two-dimensional motion, LEV and TEV are independently generated, and their interaction is very weak.

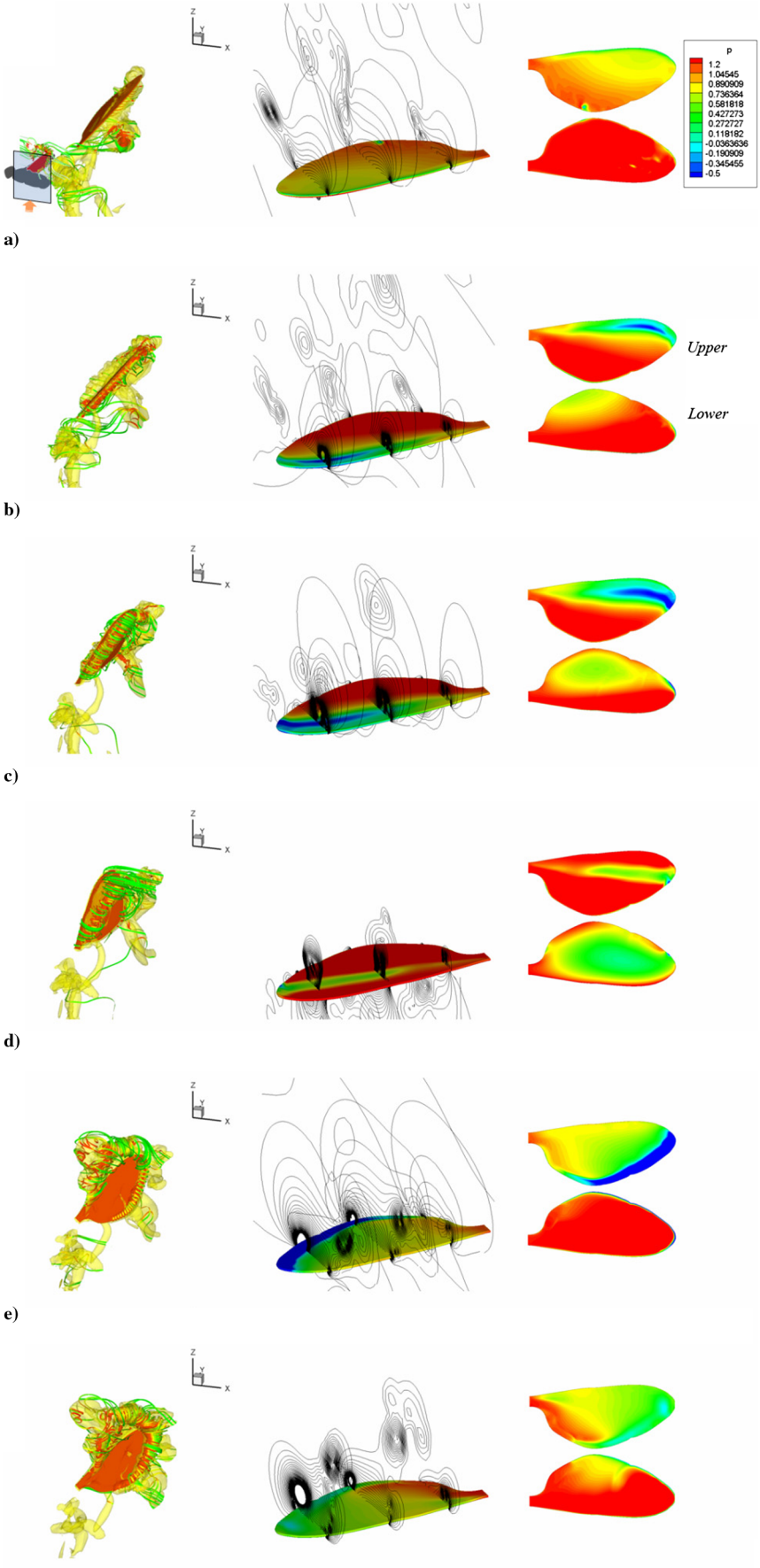

Fig. 23 Vorticity (left), cross-sectional pressure field (middle), and surface pressure (right) at the end of upstroke: a) $t = 4.87T$, b) $t = 4.92T$, c) $t = 4.94T$, d) $t = 4.96T$, e) $t = 5.02T$, and f) $t = 5.04T$.

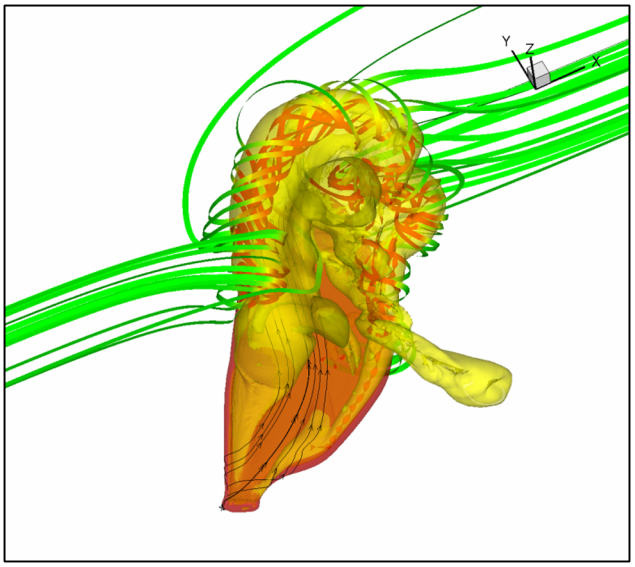

Fig. 24 Spanwise flow and LEV.

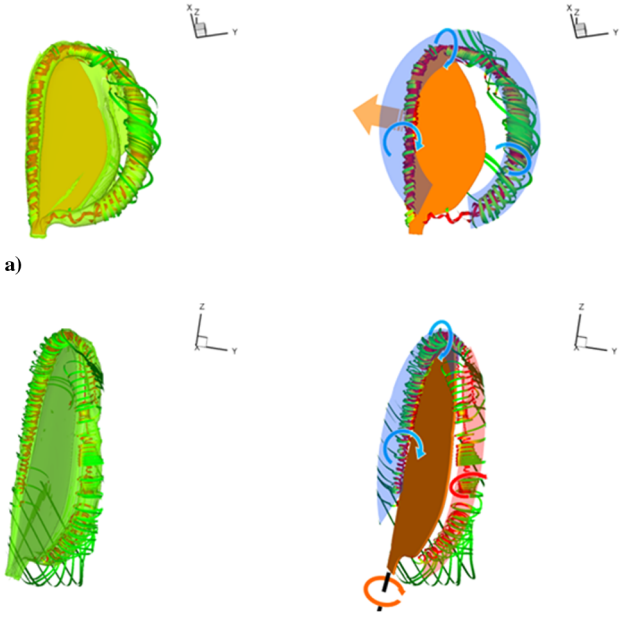

Fig. 26 Formation of vortex ring: a) translational motion is dominant and b) rotational motion is dominant.

3. *Vortex Pairing*

In two-dimensional study, vortex staying and pairing phenomena at the end of upstroke were found to be a crucial factor for impulsive thrust generation [11]. A similar pattern of vortex staying and vortex pairing can be observed in three-dimensional motion. Figure 27 shows the pairing process of two votices. First, near the end of upstroke, insect wing starts to rotate counterclockwise and translates upward, and the clockwise TEV (or part of IPVR) is generated and detached away from the lower trailing edge (Fig. 27a).

When the insect wing reaches the maximum position as in Fig. 27b, wing starts to rotate clockwise and translate downward, and a counterclockwise TEV (or part of PVR) is generated at the upper trailing edge. As the insect wing continues to translate downward, the strength of the counterclockwise TEV is increasing (Fig. 27c). Finally, the two vortices (the clockwise TEV of IPVR from the lower trailing edge and the counterclockwise TEV of PVR from the upper trailing edge) form a pairing and move into the downstream (Fig. 27d). Figure 28 shows a sectional view of vorticity field in three-dimensional motion and compares it with two-dimensional vortex pairing. It clearly shows that the two vortices induce a strong jet (Fig. 28a) similar to two-dimensional motion (Fig. 28b). Transverse momentum by the strong jet is responsible for the second thrust peak at the end of upstroke.

4. *Wake Structure*

Novel unsteady aerodynamic characteristics in insects' flapping motion come from the interaction of LEV, TEV and WTV. It triggers the formation of vortex tube and vortex ring, and eventually leads to vortex staying, vortex pairing. These flow features appear

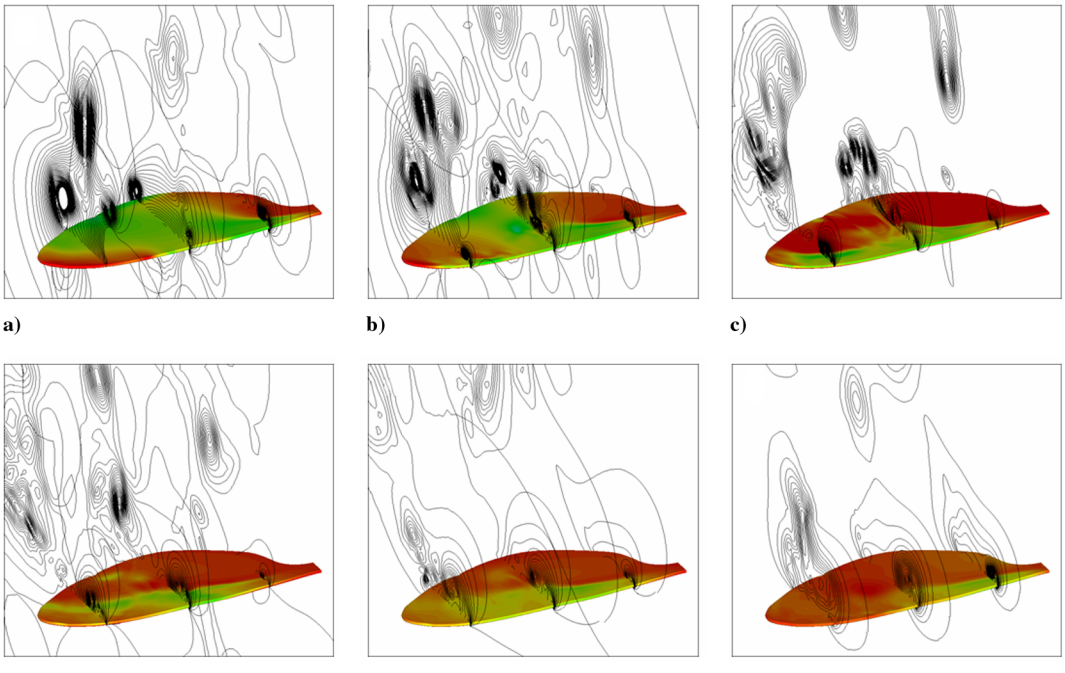

Fig. 25 Attachment and detachment of LEV and WTV during downstroke: a) $t = 4.08T$, b) $t = 4.10T$, c) $t = 4.14T$, d) $t = 4.25T$, e) $t = 4.34T$, and f) $t = 4.42T$.

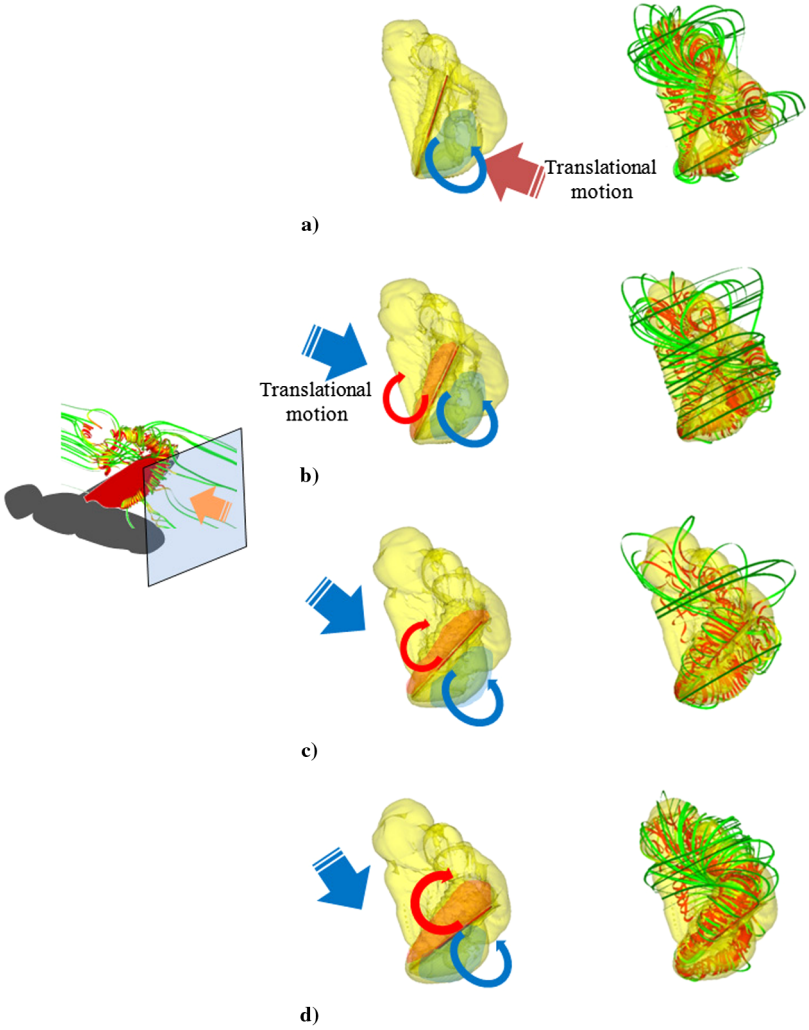

Fig. 27 Formation of three-dimensional vortex pairing.

sequentially and repeatedly during the figure-of-eight motion. As shown in Fig. 29a, at the middle of stroke, the insect wing undergoes translational motion normal to the wing surface and generates PVT or PVR. After that, PVR (or PVT) is detached from the wing, due to translational motion tangential to the wing surface (Fig. 29b). At the end of stroke, IPVR is developed due to impulsive rotation (Fig. 29c), and eventually detached from the wing due to translational motion tangential to the wing surface (Fig. 29d). These sequences of wake structures could be observed in both downstroke and upstroke. This pattern is observed only in the figure-of-eight motion with impulsive rotation at the end of strokes.

By beneficially exploiting wake and vortex structures, unsteady aerodynamics force generation of the figure-of-eight motion could be controlled. In addition, the newly uncovered flow physics provides an important clue in understanding the rapid maneuverability of insect flight, and be applied in designing flapping aerial vehicles.

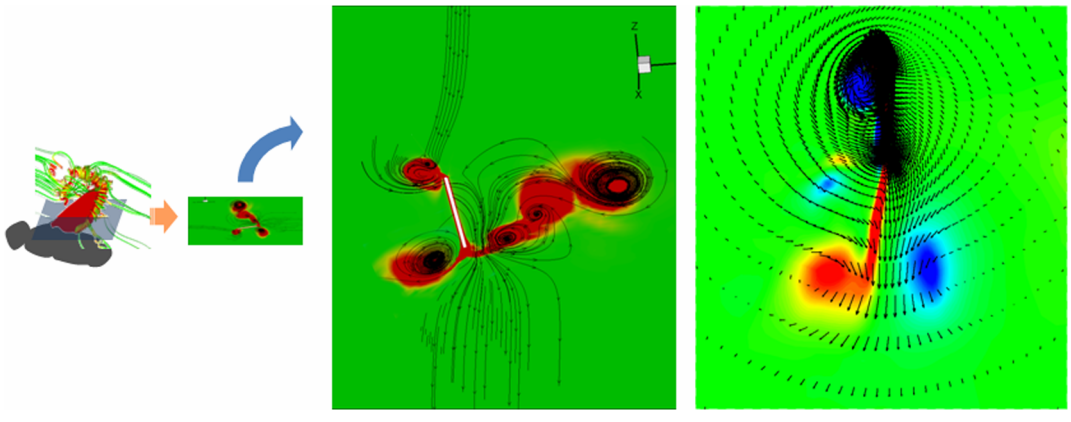

Fig. 28 Sectional view of three-dimensional vortex pairing and streamline in the wake: a) vorticity magnitude field and streamline and b) two-dimensional vortex pairing.

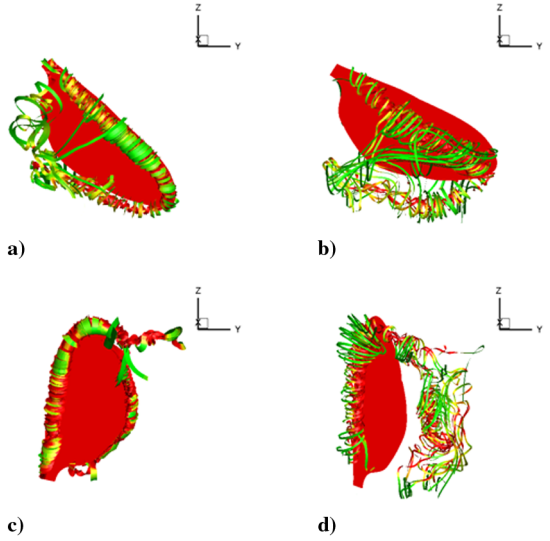

Fig. 29 Generation and detachment of vortex ring.

V. Conclusions

Computations of unsteady, viscous, incompressible flows over a thin insect wing are carried out to unveil the three-dimensional counterparts of the newly discovered vortex pairing and vortex staying under two-dimensional forward flight conditions. This is to find a physical explanation of the impulsive force generation mechanism of the insect's figure-of-eight motion under forward flight condition. Wing trajectory is extracted from data of the tethered flight experiment of a blowfly under freestream by Nachtigall [19].

Overall aerodynamic behavior is qualitatively similar to two-dimensional case: lift is generated during downstroke mainly by LEV, and thrust is impulsively generated during upstroke by complex vortex interactions. By the rapid rotation at the end of upstroke, the three-dimensional vortex staying and vortex pairing phenomena, which have been originally found in two-dimensional study, were also observed through the interaction of the PVR and the IPVR. They are responsible for the second thrust peak at the end of upstroke. Furthermore, owing to three-dimensional geometric and kinematic effects, a substantial amount of thrust (the first thrust peak) and lift is additionally generated at the middle of upstroke. In particular, the IPVR has been observed due to rapid rotational motion at the ends of up- and downstroke. These indicate that thrust and lift generation under forward flight condition due to three-dimensional effects should be taken into account for quantitative analysis.

Through three-dimensional high-fidelity analyses and its comparison with two-dimensional results, it is observed that two-dimensional analysis is a cost-effective way of capturing overall flow characteristics and the key physical phenomena. However, three-dimensional simulation is essential to obtain more quantitative results and detailed flow characteristics around the wing and the complicated vortex structures, which critically affects local aerodynamic characteristics. In this regard, two-dimensional analysis will be useful in the conceptual and preliminary design phases of micro aerial vehicles, while three-dimensional analysis is essential in the detailed design stage. Based on the present observations, efforts is in progress to investigate the effects of wing–body interaction and wing flexibility in unsteady aerodynamic force generation.

Acknowledgments

The authors wish to acknowledge financial support by the Ministry of Land, Transport, and Maritime Affairs through the Super Long Span Bridge Research and Development Center in Korea. This work was supported by the Korea Science and Engineering Foundation grant funded by the Korean government (No. 20090 084669). This work is a product of the Korea National e-Science project, and the authors also would like to acknowledge support from the KISTI Supercomputing Center (KSC-2007-S00-1016).

References

[1] Ellington, C., van den Berg, C., Willmott, A., and Thomas, A., "Leading-Edge Vortices in Insect Flight," *Nature*, Vol. 384, No. 6610, 1996, pp. 626–630. doi:10.1038/384626a0

[2] Ward-Smith, A., *Biophysical Aerodynamics and the Natural Environment*, Wiley, New York, 1984, pp. 123–142.

[3] Dickinson, M. H., and Gotz, K. G., "Unsteady Aerodynamic Performance of Model Wings at Low Reynolds Numbers," *Journal of Experimental Biology*, Vol. 174, No. 1, 1993, pp. 45–64.

[4] Dickinson, M., Lehmann, F., and Sane, S., "Wing Rotation and the Aerodynamic Basis of Insect Flight," *Science*, Vol. 284, No. 5422, 1999, pp. 1954–1960. doi:10.1126/science.284.5422.1954

[5] Yamamoto, M., and Isogai, K., "Measurement of Unsteady Fluid Dynamic Forces for a Mechanical Dragonfly Model," *AIAA Journal*, Vol. 43, No. 12, 2005, pp. 2475–2480. doi:10.2514/1.15899

[6] Okamoto, M., and Azuma, A., "Experimental Study on Aerodynamic Characteristics of Unsteady Wings at Low Reynolds Number," *AIAA Journal*, Vol. 43, No. 12, 2005, pp. 2526–2536. doi:10.2514/1.14813

[7] Sun, M., and Yu, X., "Aerodynamic Force Generation in Hovering Flight in a Tiny Insect," *AIAA Journal*, Vol. 44, No. 7, 2006, pp. 1532–1541. doi:10.2514/1.17356

[8] Liu, H., and Kawachi, K., "A Numerical Study of Insect Flight," *Journal of Computational Physics*, Vol. 146, No. 1, 1998, pp. 124–156. doi:10.1006/jcph.1998.6019

[9] Ramamurti, R., and Sandberg, W., "A Three-Dimensional Computational Study of the Aerodynamic Mechanisms of Insect Flight," *Journal of Experimental Biology*, Vol. 205, No. 10, 2002, pp. 1507–1518.

[10] Lee, J., Kim, C., and Kim, K., "Design of Flapping Airfoil for Optimal Aerodynamic Performance in Low-Reynolds Number Flows," *AIAA Journal*, Vol. 44, No. 9, 2006, pp. 1960–1972. doi:10.2514/1.15981

[11] Lee, J., Kim, J., and Kim, C., "Numerical Study on the Unsteady-Force-Generation Mechanism of Insect Flapping Motion," *AIAA Journal*, Vol. 46, No. 7, 2008, pp. 1835–1848. doi:10.2514/1.35646

[12] Platzer, M., Jones, K., Young, J., and Lai, J., "Flapping-Wing Aerodynamics: Progress and Challenges," *AIAA Journal*, Vol. 46, No. 9, 2008, pp. 2136–2148. doi:10.2514/1.29263

[13] Nagai, H., Isogai, K., Fujimoto, T., and Hayase, T., "Experimental and Numerical Study of Forward Flight Aerodynamics of Insect Flapping Wing," *AIAA Journal*, Vol. 47, No. 3, 2009, pp. 730–742. doi:10.2514/1.39462

[14] Ramamurti, R., and Sandberg, W., "A Computational Investigation of the Three-Dimensional Unsteady Aerodynamics of Drosophila Hovering and Maneuvering," *Journal of Experimental Biology*, Vol. 210, No. 5, 2007, p. 881. doi:10.1242/jeb.02704

[15] Liu, H., "Integrated Modeling of Insect Flight: From Morphology, Kinematics to Aerodynamics," *Journal of Computational Physics*, Vol. 228, No. 2, 2009, pp. 439–459. doi:10.1016/j.jcp.2008.09.020

[16] Young, J., Walker, S., Bomphrey, R., Taylor, G., and Thomas, A., "Details of Insect Wing Design and Deformation Enhance Aerodynamic Function and Flight Efficiency," *Science*, Vol. 325, No. 5947, 2009, p. 1549. doi:10.1126/science.1175928

[17] Sane, S., "The Aerodynamics of Insect Flight," *Journal of Experimental Biology*, Vol. 206, No. 23, 2003, pp. 4191–4208. doi:10.1242/jeb.00663

[18] Lehmann, F., "The Mechanisms of Lift Enhancement in Insect Flight," *Naturwissenschaften*, Vol. 91, No. 3, 2004, pp. 101–122. doi:10.1007/s00114-004-0502-3

[19] Nachtigall, W., *Insects in Flight*, McGraw–Hill, New York, 1974, pp. 38–52.

[20] Birch, J., and Dickinson, M., "The Influence of Wing-Wake Interactions on the Production of Aerodynamic Forces in Flapping Flight," *Journal of Experimental Biology*, Vol. 206, No. 13, 2003, pp. 2257–2272. doi:10.1242/jeb.00381

[21] Rogers, S., and Kwak, D., "Upwind Differencing Scheme for the Time-Accurate Incompressible Navier–Stokes Equations," *AIAA Journal*, Vol. 28, No. 2, 1990, pp. 253–262. doi:10.2514/3.10382

[22] Kim, C., Kim, C., and Rho, O., "Parallel Computations of High-Lift Airfoil Flows Using Two-Equation Turbulence Models," *AIAA Journal*, Vol. 38, No. 8, 2000, pp. 1360–1368. doi:10.2514/2.1135

[23] Brodsky, A., and Alexander, R. M., *The Evolution of Insect Flight*, Oxford Univ. Press, Oxford, 1996, pp. 35–39, 49–65.

[24] Fry, S., Sayaman, R., and Dickinson, M., "The Aerodynamics of Hovering Flight in Drosophila," *Journal of Experimental Biology*, Vol. 208, No. 12, 2005, p. 2303. doi:10.1242/jeb.01612

[25] Aono, H., Liang, F., and Liu, H., "Near- and Far-Field Aerodynamics in Insect Hovering Flight: An Integrated Computational Study," *Journal of Experimental Biology*, Vol. 211, No. 2, 2008, p. 239. doi:10.1242/jeb.008649

[26] Liu, H., and Aono, H., "Size Effects on Insect Hovering Aerodynamics: An Integrated Computational Study," *Bioinspiration and Biomimetics*, Vol. 4, No. 1, 2009, p. 015002. doi:10.1088/1748-3182/4/1/015002

[27] Birch, J., and Dickinson, M., "Spanwise Flow and the Attachment of the Leading-Edge Vortex on Insect Wings," *Nature*, Vol. 412, No. 6848, 2001, pp. 729–733. doi:10.1038/35089071

[28] Liu, H., Ellington, C., Kawachi, K., Van Den Berg, C., and Willmott, A., "A Computational Fluid Dynamic Study of Hawkmoth Hovering," *Journal of Experimental Biology*, Vol. 201, No. 4, 1998, p. 461.

Z. Wang
Associate Editor